

PSP 11-11-11
11-05-11
(C) 11-11-11COMPUTATION OF LOADS ON THE
McDONNELL DOUGLAS ADVANCED BEARINGLESS ROTORKhanh Nguyen
Aerospace Engineer
NASA Ames Research Center
Moffett Field, CADan Lauzon and Vaidyanathan Anand
Technical Staff
McDonnell Douglas Helicopter Systems
Mesa, AZ

Abstract

Computed results from UMARC and DART analyses are compared with the blade bending moments and vibratory hub loads data obtained from a full-scale wind tunnel test of the McDonnell Douglas five-bladed advanced bearingless rotor. The 5 per-rev vibratory hub loads data are corrected using results from a dynamic calibration of the rotor balance. The comparison between UMARC computed blade bending moments at different flight conditions are poor to fair, while DART results are fair to good. Using the free wake module, UMARC adequately computes the 5P vibratory hub loads for this rotor, capturing both magnitude and variations with forward speed. DART employs a uniform inflow wake model and does not adequately compute the 5P vibratory hub loads for this rotor.

Introduction

Accurate prediction of rotor loads is crucial in the development of rotor systems and has remained one of the major challenges in rotorcraft analysis. The introduction of bearingless rotor designs in recent helicopter development programs has added new challenges to the loads prediction for rotorcraft.

Bearingless rotors are characterized by the utilization of flexural members, instead of hinges and bearings, to allow the blade to flap, lead-lag, and twist. These blade motions are necessary to relieve stress and are mandatory for trim control inputs. The utilization of flexural members significantly reduces the complexity of rotor hub designs making bearingless rotors easier to maintain and to manufacture. The design simplicity of these rotors complicates the analysis of rotor aeroelasticity due to redundant load paths, complex bending-torsion and geometrical couplings, and material nonlinear characteristics.

The major components of a modern bearingless rotor are the blades, the flexbeam, the pitchcase, and the snubber damper assemblies. The flexbeam is a flexural member connecting the blade to the rotor hub and allows the blade to flap, lead-lag, and twist. The pitchcase encloses the flexbeam and connects the blade to the control system allowing the transfer of pitch inputs to the blade. The inboard end of the pitchcase is connected to the snubber-damper assembly. The snubber acts as a pivot for the flap motions and allows the pitchcase to rotate in pitch. The snubber also reacts the majority of the pitch-link load and provides a load path for the pitchcase vertical and shear forces to the hub. A pair of shear lag dampers, made of elastomeric materials, is mounted between the snubber and the pitchcase to provide auxiliary damping to the blade inplane motions.

The computation of rotor loads is an aeroelastic problem involving the complex interaction between the aerodynamic, inertia, and elastic forces and moments. In response to the aerodynamic environment at the rotor, the blade undergoes periodic motions which in turn are fed back as a source of input generating the higher harmonic airloads. In addition, the temporal and spanwise variations in the blade airloads create a system of shed and trailed vorticities behind each blade, in the vicinity of the rotor disk. The vortex system induces an unsteady nonuniform inflow which directly affects the local blade angle of attack and in turn, influences the blade airloads. For certain flight conditions, close blade-vortex interaction is also another source of higher harmonic airloads. Therefore, accurate computation of the higher harmonic rotor loads requires aerodynamic modeling that includes nonuniform inflow calculation and representations for nonlinear unsteady aerodynamic effects.

Adding to the complexity of the load calculation, modeling of a bearingless rotor has added new challenges to the structural dynamics discipline. Structural modeling of a bearingless blade must include representation of redundant load paths, while the effects of nonlinear kinematic couplings and nonlinear damper behavior are important and must be included for some bearingless configurations. The finite element methodologies presented in Refs. 1 to 3 are capable of simulating the geo-

metric complexities of bearingless rotors. However, an extension to the modal approach using the transfer matrix approach has been shown in Refs. 4 to 6 to be quite successful in modeling bearingless rotors.

While the amount of research dealing with loads computation for articulated or hingeless rotors is quite extensive, there is limited literature addressing the computation of loads on bearingless rotors. References 7-9 present comparisons between computed results using Bell Helicopter Textron's COPTER analysis and the loads data obtained from their bearingless rotor designs. Flight test data from the HARP bearingless rotor were used in the correlation studies using DART (Dynamics Analysis Research Tool) and RACAP analyses from McDonnell Douglas Helicopter Company (MDHC) (Refs. 10,11). Reference 5 presented the correlation of the blade bending moments calculation of the Sikorsky SBMR using UMARC (University of Maryland Advanced Rotor Code) and Sikorsky's KTRAN analyses with full-scale wind tunnel data. Wind tunnel data from a five-bladed scale model rotor were compared with Boeing's TECH-01 analytical results in Ref. 4.

This paper presents the results of a validation study comparing the loads data acquired from the McDonnell Douglas Advanced Rotor Technology (MDART) test program and the computed results of the UMARC and DART analyses. The focus of this validation study is to evaluate the ability of the two analyses in computing blade bending loads and vibratory rotor hub loads for a modern bearingless rotor in hover and forward flight.

MDART Test Hardware and Data Reduction

References 12 and 13 describe the overall MDART wind tunnel test program, and Ref. 14 presents the aeroelastic stability data and the comparison with results of the UMARC and DART analyses. The correlation results of Ref. 14 indicate that both analyses perform well in computing the aeroelastic stability of the MDART rotor in both hover and forward flight conditions.

The MDART rotor is a modern five-bladed bearingless design and was tested in the NASA Ames 40- by 80-Foot Wind Tunnel. The joint NASA-McDonnell Douglas MDART test program aimed to measure the rotor aerodynamic performance, control derivatives, blade and hub loads, control power requirements, aeroelastic stability, acoustic characteristics, and responses to higher harmonic control inputs. The MDART rotor was tested from hover to airspeeds in excess of 200 kts and up to 10,000 lb of thrust, corresponding to a thrust coefficient to solidity ratio (C_T/σ) of 0.13. The rotor was fully instrumented, including blade strain gauges for flapwise and chordwise bending and torsional moments, pitch-link

and control system loads, and rotor steady and vibratory hub loads.

The MDART rotor is a soft-inplane bearingless rotor and is a pre-production rotor for the MD Explorer. The rotor has a 34-foot diameter and 3 deg of precone which starts from the flexbeam-hub attachment location. The nominal rotor thrust is 5800 lb, and the design cruise speed is 150 kts. The modern HH-10 airfoil extends from the blade attachment to the 74 percent blade radial station, from which the blade cross section undergoes a region of airfoil transition covering 10 percent of the blade radius. The HH-06 airfoil forms the remaining part of the blade tip region. The blade chord is a constant 10 in which is swept into a parabolic leading edge shape at the tip for performance and acoustic benefits. The blade has -10 deg of blade pretwist (twist down from root to tip). The flexbeam extends from the hub to 20 percent of the overall blade radius and is of rectangular cross-section. The inboard part of the flexbeam transitions into two flat legs which are bolted to the hub in an over-under arrangement. The pitchcase encloses the flexbeam and is of an elliptical cross-section. The snubber is attached to the hub via an elastomeric bearing. A pair of elastomeric dampers mounts to both ends of the snubber, shears against the chordwise motions of the pitchcase, and provides auxiliary damping to the blade inplane motions.

During the test program, the rotor was installed on the McDonnell Douglas Large Scale Dynamic Rig (LSDR). The LSDR lower housing contained a 1500 hp electric motor and transmission system. The upper housing contained the rotor balance and the hydraulic servo-actuators for the control system. The five-component rotor balance measured both steady and vibratory hub loads which included the axial, side, and normal forces, and the rolling and pitching moments. The rotor hub was connected to the static mast which was then mounted to the rotor balance. The static mast enclosed the rotating drive shaft that transferred torque to the rotor hub. In this arrangement, the static mast transferred the rotor hub forces and rolling and pitching moments directly to the rotor balance.

Both static and dynamic data were acquired during the test program. The raw dynamic data were sampled at 64 per rotor revolution and were passed through a four-pole Bessel filter with a bandwidth of 100 Hz. Eight revolutions of data were harmonically analyzed, and ten harmonics of the reduced data were saved in the database.

Dynamic Calibration

The dynamic calibration of the LSDR's rotor balance was performed in the test section of the 40- by 80-Foot Wind Tunnel prior to the rotor installation. A hydraulic actuator excited a rigid 28-in diameter circular

plate that acted as a simulated hub. A load cell, mounted between the actuator and the simulated hub, measured the actuator force. A shaker controller, operated in the stroke feedback mode, provided broadband random excitation to the actuator. A signal analysis system acquired the data and computed the balance frequency responses on-line. The frequency responses related the balance axial, side and normal forces, and the rolling and pitching moments to the load cell signal. To reduce the influence of sensor noise, 40 data averages were used in the computation of the frequency responses.

In the dynamic calibration, seven shaking configurations were employed: two inplane shakes in the longitudinal and lateral directions providing axial force-pitching moment and side force-rolling moment inputs and five vertical shakes. One of the vertical shakes was at the hub center, providing a pure vertical force input. For the other four vertical shakes, the excitation location was offset by 13.6 in from the hub centerline at the fore and aft positions providing two independent vertical force-pitching moment inputs and at the two sides of the plate providing another two independent vertical force-rolling moment inputs. In fact, five independent shaking configurations were necessary to determine the balance dynamic calibration matrix. However, seven shaking configurations were applied to help reduce the effects of sensor noises and uncertainties in the test set up, such as misalignment of the hydraulic shaker.

The balance transfer function values at 32.7 Hz, corresponding to the 5 per rev (5P) frequency of the MDART rotor, were extracted from the signal analysis system to yield the frequency response matrix. The response matrix was included along with an input matrix in the computation of the balance dynamic calibration matrix. The input matrix contained information about the shake direction and the moment arm. The dynamic calibration matrix was computed using a least-squares method. The resulting dynamic calibration matrix included the dynamic couplings between the balance load component signals as well as the magnitude and phase corrections for these components.

The dynamic calibration was conducted with the rotor shaft vertical and non-rotating. The effects of the rotor shaft tilt on the dynamic calibration results, which might be significant, were not investigated. The effects of shaft rotation on the dynamic calibration results were expected to be small, as shown in Ref. 15 for another full-scale rotor balance system, and due to the unique arrangement of the rotor test stand that allows a direct transfer of rotor hub loads to the balance through a static mast.

Sample results of the dynamic calibration are presented in Figs. 1 to 3 which show the variations of the measured and corrected 5P axial, side, and normal forces

magnitudes with forward speed, respectively. The vibratory hub forces are nondimensionalized by 30,700 lbs and the hub moments by 520,000 ft-lbs. The results from Fig. 2 indicate that the balance side force signal was amplified by a factor of four by the 5P side force excitation. The amplification factors for the 5P axial and normal forces were moderate, as shown in Figs. 1 and 3, respectively. The dynamic couplings between the balance force components were small, while the dynamic couplings between the moments and the inplane forces were large and were due mainly to the vertical offset between the balance center and the hub.

Analytical Model

UMARC is a finite element code which includes advanced unsteady aerodynamics and vortex wake modeling. The code was developed at the University of Maryland. DART is the standard rotor dynamics analysis code at MDHC and was used extensively in the design and development of the MDART rotor, as well as the Apache and the MD 500 rotor systems. DART is capable of analyzing a wide range of structural dynamic problems, including aeromechanical analysis of rotors with redundant load paths.

UMARC Analysis

UMARC models the rotor blade as an elastic beam, undergoing flap and lead-lag bending, elastic twist, and axial deflection. The finite element method based on Hamilton's principle is employed to discretize the blade into a finite number of beam elements. Each beam element has fifteen degrees-of-freedom and consists of two end nodes and three internal nodes. The six degrees-of-freedom at each end node are: displacements and slopes for the flap and lead-lag bending, and displacements for the elastic twist and axial deflection. There are two internal nodes for the axial degree-of-freedom, and one internal node for the elastic twist motion. The formulation of the governing equations is developed for nonuniform blades having pre-twist, pre-pitch, precone, and chordwise offsets from the blade pitch axis for the loci of the center-of-mass and aerodynamic center, and the tensile and elastic axes.

The blade boundary conditions and the connectivity between beam elements were incorporated into UMARC to model the MDART rotor. The blade and flexbeam formed one load path connected to the hub, and the pitchcase formed another load path connecting the blade to the control system and the snubber-damper assembly. The blade is modeled with nine beam elements, while the flexbeam and pitchcase are modeled by eight and three beam elements, respectively. Structural properties are uniform across the beam elements. The flexbeam is cantilevered to the hub. The pitchcase inboard end is free, restrained by the snubber-damper assembly and the pitchlink, modeled as discrete springs and linear viscous

dampers. At the blade-flexbeam-pitchcase connection, continuity of displacements and slopes for flap and lead-lag bending and displacements for elastic twist and axial deflections was imposed.

The airloads were calculated using a nonlinear unsteady aerodynamic model based on the works of Leishman and Beddoes (Ref. 16). This model consists of an attached compressible flow (linear) formulation along with a representation of the nonlinear effects due to trailing edge flow separation and dynamic stall. The flow separation model was based on Kirchhoff's formulation which relates the flow separation point to the airfoil force and moment behavior. The static airfoil table allows the representation of the variation of the separation point with angle of attack with a single curve fit. Information about the flow separation point allow the reconstruction of the airfoil static behavior, a precursor to the modeling of the airfoil dynamic characteristics. The curve fitting process was applied using HH-10 and HH-06 airfoil tables.

For inflow calculations, a prescribed wake was used for hover and a modified free wake model was used for forward flight conditions. Both wake models were originally adapted from CAMRAD (Ref. 17). The modification in the CAMRAD free wake model aimed to improve the convergence behavior of the wake geometry computation by using a predictor-corrector updating scheme with non-reflective periodic boundary conditions.

The coupled blade responses and the trim control settings were solved for wind tunnel conditions. The rotor shaft orientation was set to the test condition value, and the rotor was trimmed to a prescribed thrust and steady hub moments. The blade section bending moments were calculated using the modal summation method, while the rotor hub loads were calculated using the force summation method.

DART Analysis

DART analyzes the dynamics of multiple degrees of freedom connected through masses, dampers, springs and linear constraints. Such a system can be analyzed for stability, natural vibration characteristics, and transient responses. The DART transient analysis is capable of including nonlinear effects, such as stall, as well as the effects of periodic coefficients.

Specialized structural and aerodynamic modules are available to accept rotor blade input specifications in a standard format and then convert them into appropriate models accessible by the core program. The results represent the discretized dynamics due to the coupled flap-lag-torsion deformation of a rotor blade.

The structural pre-processor automatically generates a standard model for the primary load along the blade for

five coupled motions at each blade radial station: displacements and slopes for flap and lead-lag, and torsion displacement. The analyst completes the model by filling in the connections between the blade root and the hub as appropriate to the rotor. For the MDART rotor, the standard model is continued inboard along the flexbeam to the hub with 15 stations. The additional load paths are then modeled by adding elements that connect the blade root to the pitchcase, the snubber-damper assembly and the hub on one side, and the pitchcase to the pitch link and control input on the other side. Two stations are used to model the pitchcase.

The airloads were computed using the nonlinear aerodynamic options in DART. This module included an airfoil table look-up, reverse flow effects, and a representation for dynamic stall. A lift deficiency function, which is a close approximation to the classical Theodorsen's function, was used to capture the unsteady potential flow effects. The rotor inflow was calculated using momentum theory.

The set of ordinary differential equations resulting from the model assembly were solved using a time integration scheme with the rotor trim settings automatically adjusted to a target thrust, trim flap angles, and torque values. Periodicity of the blade response solutions as well as the matching of rotor trim conditions determined the convergence of the overall solutions.

Results and Discussion

The correlation between computed results using the UMARC and DART analyses and experimental data obtained from the MDART rotor test program are presented. The first set of results includes the blade bending moments in both hover and forward flight conditions. The second set of results show the 5P vibratory hub loads correlation.

Blade Bending Moments

The bending moment distributions are for the blade and flexbeam sections. Note that the flexbeam extends from the hub to the blade station 41, which is identical to the blade attachment location. Note that the blade station numbers are expressed in inches. The blade and flexbeam were instrumented with flapwise bridges at stations 9, 42.75, 70, 87, 120, 164, 181; chordwise bridges at stations 19.5, 42.75, 70, 120, 152. The mean data were corrected for a gravity tare computed for a nonrotating blade, while the effects of rotation on the strain gauge signals were not addressed. Only the mean data are presented in hover, and both mean and vibratory data are presented for the forward flight conditions. The vibratory blade loads include harmonics from one to ten.

Figure 4 shows the radial distribution of the mean blade bending moments at the test condition of 4 deg

collective pitch in hover. The results shown in Fig. 4a indicate that DART analysis captures the flap bending moment fairly well at this flight condition, especially for the inboard region. UMARC can only capture the trend in flap bending distribution for the mid-span region and gives the wrong trend in the inboard region. Both analyses fail to capture the sharp rise in load outboard near the blade tip. For the chordwise bending moments (Fig. 4b), the results from both analyses are fair for the outboard blade region and poor in the inboard region. In particular, both analyses fail to capture the chordwise bending moment variation at the blade-flexbeam junction.

The correlation results in hover at the 9 deg collective pitch, the nominal thrust condition for the MDART rotor ($C_T/\sigma = .076$), are shown in Fig. 5. Computed results from both analyses correlate well with the flap bending moment for the inboard portion of the blade (Fig. 5a). The correlation is fair over the blade mid span, and both analyses capture somewhat the peak in flapwise bending moment near the blade tip. DART results match well with the chordwise bending moment data (Fig. 5b), except for the mid span station. UMARC results are reasonable for this flight condition.

The blade bending moment results at 83 kts ($\mu = 0.2$) and nominal thrust ($C_T/\sigma = 0.076$) are shown in Figs. 6 and 7. Figure 6a shows the mean flapwise bending moment, while Fig. 6b shows the vibratory (half peak-to-peak) components. The results in Fig. 6a indicate that the DART results correlate well with the mean flapwise bending moment over the whole blade section. UMARC results are fair and miss the peaks near the blade tip and at the blade attachment location. For the vibratory flapwise bending moments, the results from both analyses are fair with UMARC capturing the peak at the blade attachment location better than DART.

Figure 7a shows the mean chordwise variation. Again, the correlation between analytical results and experimental data are fair and exhibits a trend similar to that seen in Fig. 4b for the low collective hover test condition shown earlier. The results of Fig. 7b show that both analyses perform fairly in the computation of the vibratory chordwise bending moment. Over most of the blade span, UMARC slightly overpredicts the data, while DART slightly underpredicts the data.

Figures 8 and 9 present the blade bending moments for the flight condition of 155 kts ($\mu = 0.37$) and nominal thrust, which represents the design cruise condition for the MDART rotor. The mean flapwise bending moments shown in Fig. 8a indicate that the DART results compare very well with experimental data. UMARC results are fair, failing to capture the peak near the blade tip similar to the results shown in Fig. 6a. The vibratory flapwise bending moment data are captured quite

well by both analyses (Fig. 8b), with DART slightly overpredicting and UMARC slightly underpredicting the data.

Figure 9a shows the mean chordwise bending moment for the cruise flight condition. The results from both analyses are reasonable, with DART providing a slightly better correlation with the data. DART results for the vibratory chordwise bending moment are excellent, while UMARC overpredicts the data over the entire blade span.

Vibratory Hub Loads

The correlation of the rotor 5P hub loads data with analytical results are shown next. The 5P rotor hub loads are dynamically corrected and represent the nonrotating hub loads in the fixed system. Only the magnitudes of the vibratory hub loads are shown, and the results are nondimensionalized. The results are presented over the range of advance ratios at the nominal thrust of the MDART rotor. Table 1 presents the rotor operating conditions. The sign convention for the shaft tilt angle is positive back, and those for positive hub rolling and pitching moments are advancing side down and nose up, respectively. The shaft tilt angle schedule was set to simulate the steady level flight conditions of the MD Explorer. UMARC 5P hub loads results were obtained with the free wake model, while DART used a uniform inflow model.

Figure 10 shows the 5P hub axial force magnitude of the MDART rotor as a function of advance ratio. The experimental data shows that this 5P hub load component is high in the transition flight condition ($\mu = 0.08$). The 5P axial force drops as the forward speed increases to an advance ratio of 0.15 and starts increasing at the higher forward speed. The largest increase in the 5P axial force occurs in the high speed region, between the advance ratios of 0.35 to 0.37. The correlation between UMARC results and the data for the 5P axial force is excellent, capturing the trend very well. The DART analysis completely underpredicts the 5P axial force, although the trend is reasonably well captured in the high forward speed region (μ greater than 0.2). Since the rotor nonuniform inflow in the transition flight regime is a source of higher harmonic airloads, the inability of the DART analysis to capture the variation of the 5P axial force in this flight regime is due to a lack of a vortex wake model.

The results for the 5P hub side force are shown in Fig. 11. UMARC shows a variation and magnitude of the 5P side force virtually identical to the axial force calculation shown in Fig. 10; UMARC completely overpredicts the experimental data shown in Fig. 11. The DART results match the data quite well, except in the transition flight regime.

The variation of the 5P hub normal force with forward speed is shown in Fig. 12. The data exhibit a large 5P component for advance ratios from .08 to 0.15. As the forward speed increases, the 5P normal force reduces until an advance ratio of 0.2 and thereafter remains relatively constant at the higher forward speeds. Both analysis fail to capture the variation of the 5P normal force with forward speed, with UMARC results being closer in magnitude to the data than the DART results.

The results for the 5P hub rolling and pitching moments are shown in Figs. 13 and 14, respectively. The data for both cases show large components in the transition flight regime, decreasing to a minimum and then increasing with increasing forward speed. Both of these trends and magnitudes of the data are captured by the UMARC results. DART results only capture the trends at the high forward speed and grossly underpredict the magnitudes over the complete speed range.

Conclusions

Test data obtained from a full-scale test of a advanced five-bladed bearingless rotor are used in a validation study using the UMARC and DART analyses. The study compares the computed mean and vibratory blade loads and the 5P vibratory hub loads with experimental data. The vibratory hub loads are corrected using results from a dynamic calibration of the rotor balance.

The results for the mean blade loads correlation indicate that the UMARC computation is fair to poor at the low collective and is fair at the high collective pitch in hover. DART results for the same conditions are fair. In forward flight, UMARC results are fair in the computation of the mean and vibratory flapwise bending moment and remain poor for both mean and vibratory chordwise bending moments. DART results are good for the mean and fair for the vibratory flapwise bending moment. DART computation of the mean and vibratory chordwise bending moment are fair.

For the 5P hub loads calculation, UMARC results are good for the axial force and rolling and pitching moments, poor for the side force, and fair for the normal force. The overall DART results are poor and underestimate the 5P hub loads components, except for the 5P side force calculation. Also, DART only captures the trend in the 5P hub loads variation at the high forward speed and fails to capture the trend in the transition flight regime.

References

1. Ormiston, R. A., Ruzicka, G. C., Jung, Y., and Saberi, H., "Comprehensive Aeromechanics Analysis of

- Complex Rotorcraft Using 2GCHAS," American Helicopter Society Aeromechanics Specialists Conference, San Francisco, CA, Jan 1994.
2. Johnson, W., "Technology Drivers in the Development of CAMRAD II," American Helicopter Society Aeromechanics Specialists Conference, San Francisco, CA, Jan 1994.
3. Chopra, I. and Bir, G., "University of Maryland Advanced Rotor Code: UMARC," American Helicopter Society Aeromechanics Specialists Conference, San Francisco, CA, Jan 1994.
4. Shultz, L. A., Panda, B., Tarzanin, F. J., Derham, R. C., Oh, B. K., and Dadone, L., "Interdisciplinary Analysis for Advanced Rotors - Approach, Capabilities and Status," American Helicopter Society Aeromechanics Specialists Conference, San Francisco, CA, Jan 1994.
5. Wang, J. and Norman, T., "Correlation of Flatwise and Chordwise Bending Moments for a Sikorsky Full-Scale Bearingless Main Rotor," American Helicopter Society Aeromechanics Specialists Conference, San Francisco, CA, Jan 1994.
6. Murthy, V. R. and Joshi, A. M., "Free Vibration Characteristics of Multiple Load Path Blades by the Transfer Matrix Method," *Journal of the American Helicopter Society*, Vol. 31, (4), Oct 1986.
7. Corrigan, J. J., Schillings, J. J., and Yin, S. K., "Development in Dynamics Methodology at Bell Helicopter Textron," American Helicopter Society 44th Annual Forum, Washington, D.C., Jun 1988.
8. Yen, J. G., Yuce, M., Chao, C. F., and Schillings, J. J., "Validation of Rotor Vibratory Airloads and Application to Helicopter Response," *Journal of the American Helicopter Society*, Vol. 35, (4), 1990.
9. Yen, J. G. and Yuce, M., "Correlation of Pitch-Link Loads in Deep Stall on Bearingless Rotors," *Journal of the American Helicopter Society*, Vol. 37, (4), Oct 1992.
10. Sorensen, J. L., Silverthorn, L. J., and Maier, T. H., "Dynamic Characteristics of Advanced Bearingless Rotors at McDonnell Douglas Helicopter Company," American Helicopter Society 44th Annual Forum, Washington, D.C., Jun 1988.
11. Sangha, K. B., "Bearingless Rotors and Higher Harmonic Control Modeling Using RACAP," American Helicopter Society 44th Annual Forum, Washington, D.C., Jun 1988.
12. McNulty, M., Jacklin, S., and Lau, B., "A Full-Scale Test of the McDonnell Douglas Advanced Bearingless Rotor in the NASA Ames 40 X 80 Foot Wind Tunnel," American Helicopter Society 49th Annual Forum, St. Louis, MO, May 1993.
13. Jacklin, S., Lau, B., Nguyen, K., Smith, R., and McNulty, M., "Full-Scale Wind Tunnel Test of the McDonnell Douglas Five-Bladed Advanced Bearingless Rotor: Performance, Stability, Loads, Control Power, Vibration, and HHC Data," American Helicopter Society Aeromechanics Specialists Conference, San Francisco, CA, Jan 1994.
14. Nguyen, K., McNulty, M., Anand, V., and Lauzon, D., "Aeroelastic Stability of the McDonnell Douglas Advanced Bearingless Rotor," American Helicopter Society 49th Annual Forum, St. Louis, MO, May 1993.
15. van Aken, J., Peterson, R. L., and Freedman, C. J., "Calibration Results of the NASA Ames Rotor Test

- Apparatus Steady/Dynamic Rotor Balance," American Helicopter Society Aeromechanics Specialists Conference, San Francisco, CA, Jan 1994.
16. Leishman, J. G., and Beddoes, T. S., "A Semi-Empirical Model for Dynamic Stall," *Journal of the American Helicopter Society*, Vol. 1, (3), Jul 1989.

17. Johnson, W., "A Comprehensive Analytical Model of Rotorcraft Aerodynamics and Dynamics, Part I: Analysis and Development," NASA TM-81182, Jun 1980.

Table 1 MDART Rotor Operating Trim Condition for Forward Speed Sweep

| Airspeed (kts) | Advance Ratio | Shaft Tilt (deg) | Thrust (lbs) | Rolling Moment (in-lbs) | Pitching Moment (in-lbs) |
|-------------------|------------------|---------------------|-----------------|----------------------------|-----------------------------|
| 33.2 | .0801 | -1.1 | 5831 | 3979 | -4971 |
| 62.5 | .1512 | -2.6 | 5828 | 5305 | -2600 |
| 82.6 | .1996 | -4.9 | 5660 | 3836 | -4275 |
| 102.8 | .2484 | -6.9 | 5737 | 3634 | -3895 |
| 123.2 | .2987 | -8.8 | 5847 | 6492 | 642 |
| 144.3 | .3491 | -10.9 | 5609 | 6718 | -2399 |
| 154.8 | .3729 | -11.8 | 5591 | 11393 | 1234 |

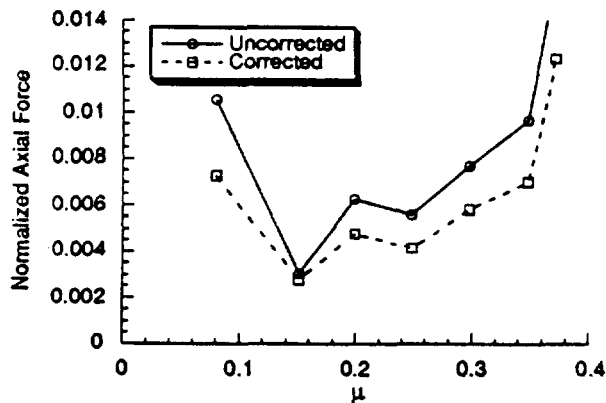


Fig. 1 Comparison of uncorrected and dynamically corrected 5P axial force, variation with forward speed at $C_T/\sigma = .076$.

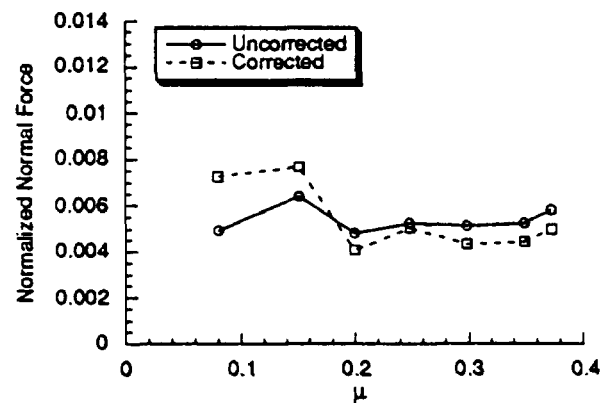


Fig. 3 Comparison of uncorrected and dynamically corrected 5P normal force, variation with forward speed at $C_T/\sigma = .076$.

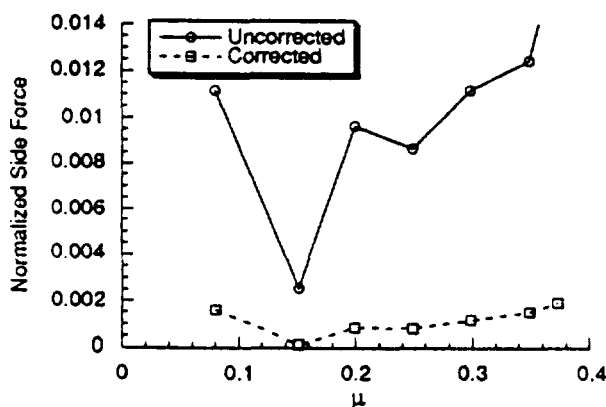


Fig. 2 Comparison of uncorrected and dynamically corrected 5P side force, variation with forward speed at $C_T/\sigma = .076$.

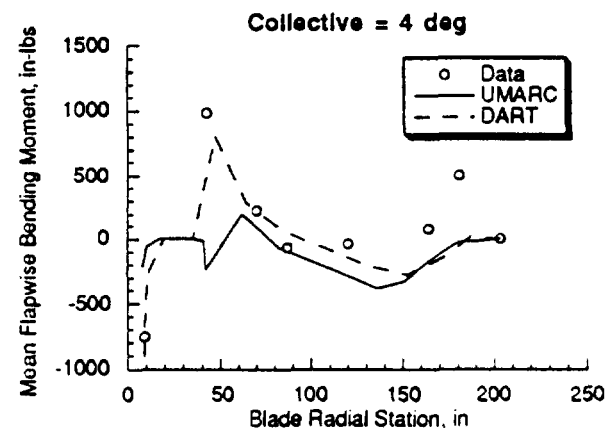


Fig. 4a Comparison of measured and computed blade and flexbeam flapwise bending moment in hover, collective pitch = 4 deg.

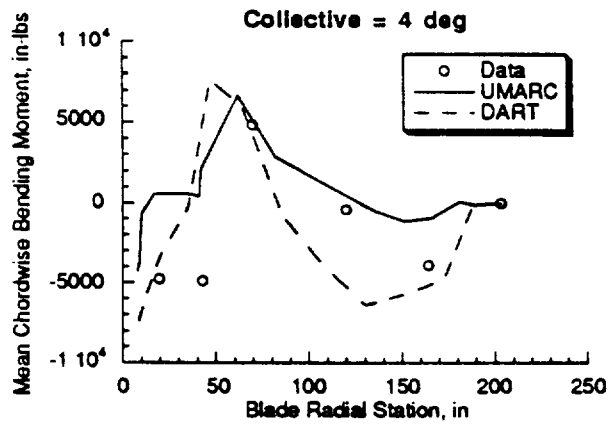


Fig. 4b Comparison of measured and computed blade and flexbeam chordwise bending moment in hover, collective pitch = 4 deg.

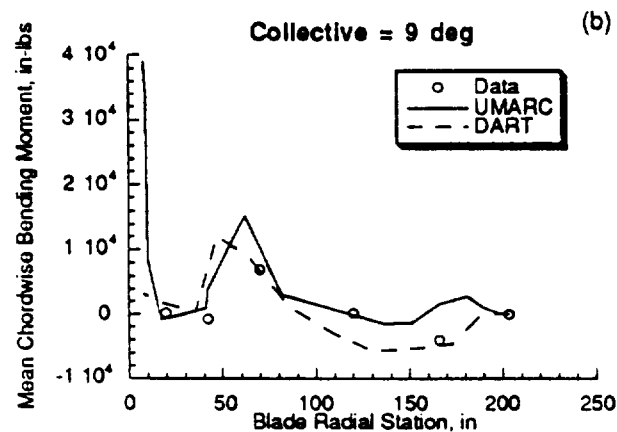
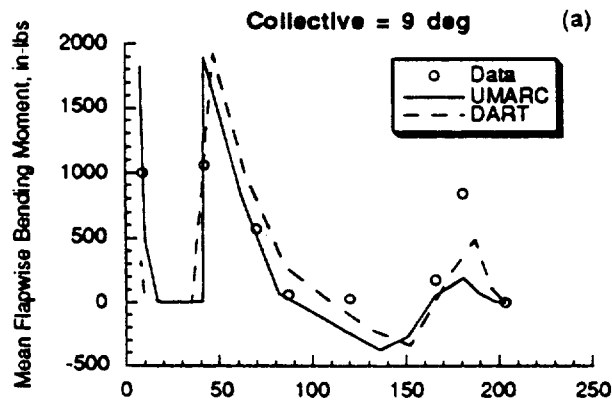


Fig. 5 Comparison of measured and computed blade and flexbeam (a) flapwise and (b) chordwise bending moment in hover, collective pitch = 9 deg.

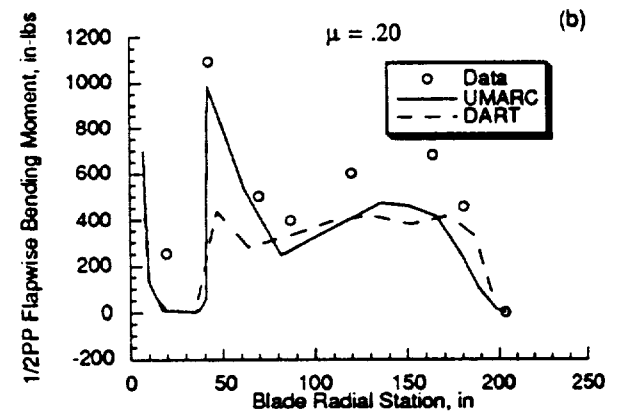
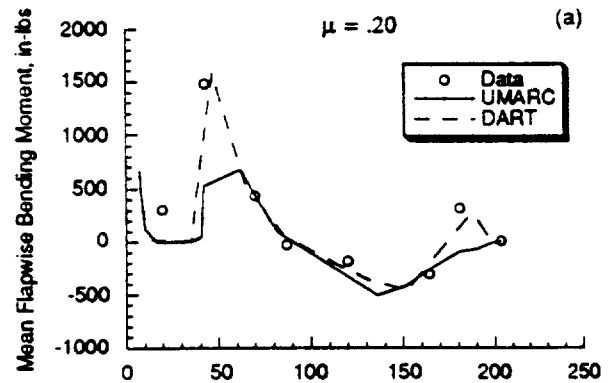


Fig. 6 Comparison of measured and computed (a) mean value and (b) half peak-to-peak value of blade and flexbeam flapwise bending moment in forward flight ($C_T/\sigma = .076$, $\mu = .20$).

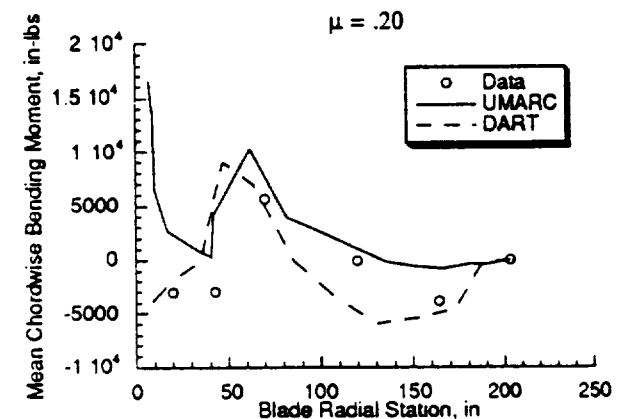


Fig. 7a Comparison of measured and computed mean blade and flexbeam chordwise bending moment in forward flight ($C_T/\sigma = .076$, $\mu = .20$).

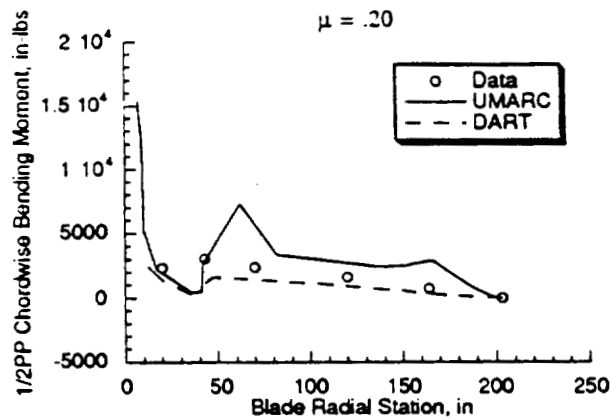


Fig. 7b Comparison of measured and computed half peak-to-peak blade and flexbeam chordwise bending moment in forward flight ($C_T/\sigma = .076$, $\mu = .20$).

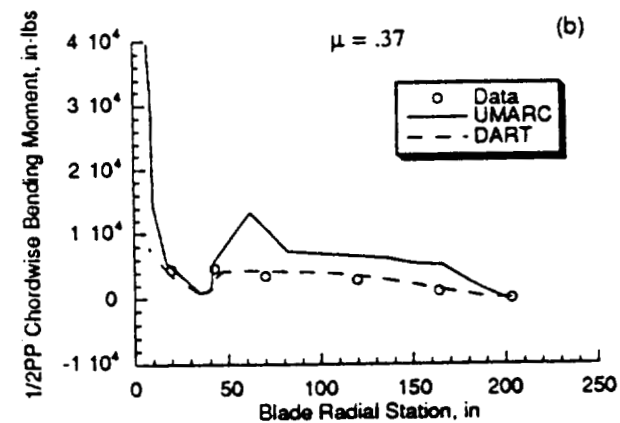
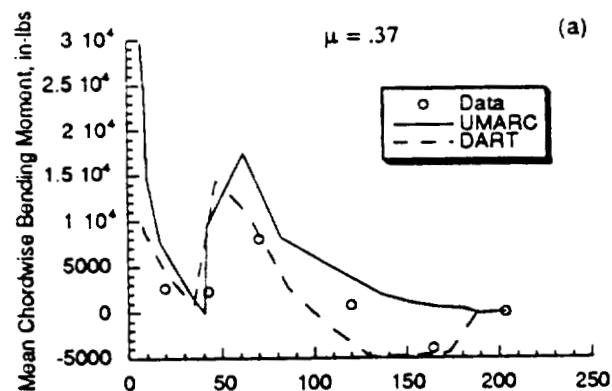


Fig. 9 Comparison of measured and computed (a) mean value and (b) half peak-to-peak value of blade and flexbeam chordwise bending moment in forward flight ($C_T/\sigma = .076$, $\mu = .37$).

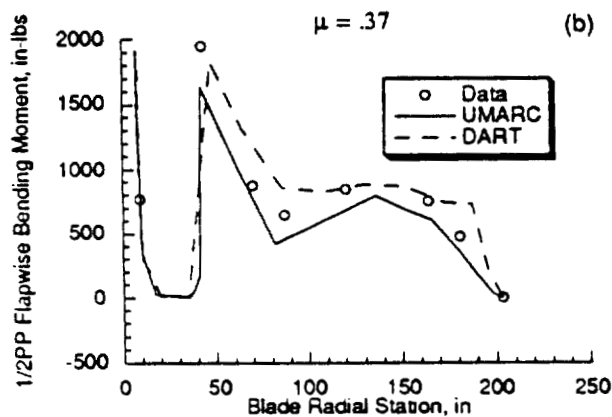
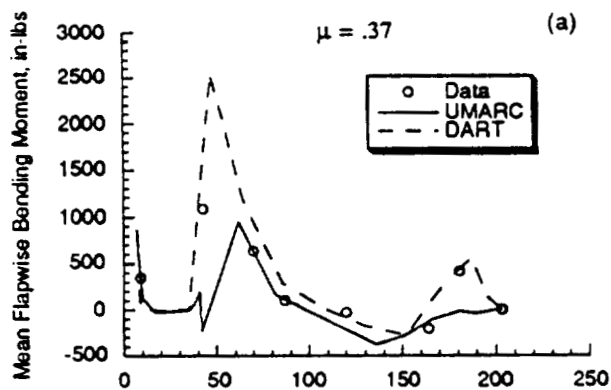


Fig. 8 Comparison of measured and computed (a) mean value and (b) half peak-to-peak value of blade and flexbeam flapwise bending moment in forward flight ($C_T/\sigma = .076$, $\mu = .37$).

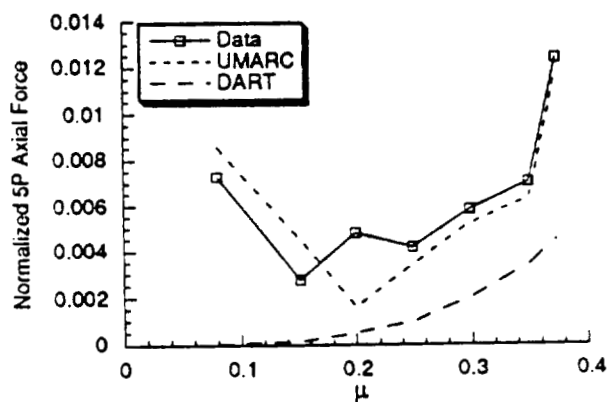


Fig. 10 Comparison of 5P axial force data with DART and UMARC results, variation with forward speed at $C_T/\sigma = .076$.

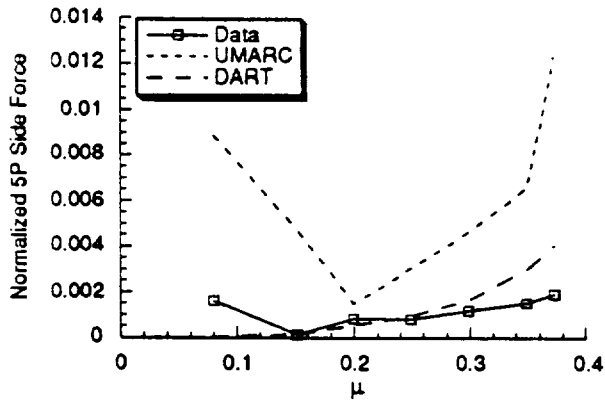


Fig. 11 Comparison of 5P side force data with DART and UMARC results, variation with forward speed at $C_T/\sigma = .076$.

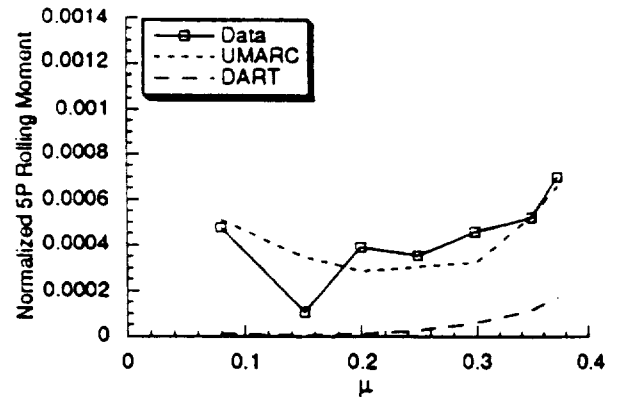


Fig. 13 Comparison of 5P rolling moment data with DART and UMARC results, variation with forward speed at $C_T/\sigma = .076$.

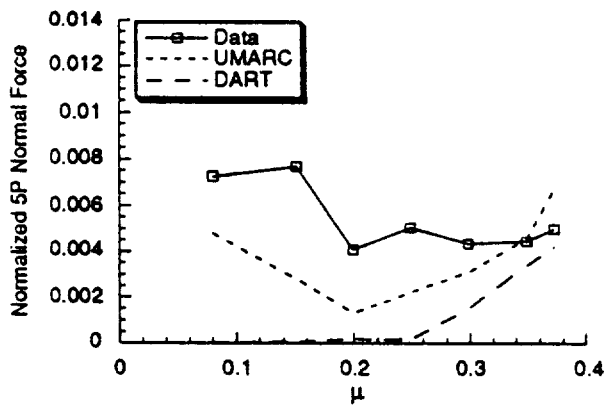


Fig. 12 Comparison of 5P normal force data with DART and UMARC results, variation with forward speed at $C_T/\sigma = .076$.

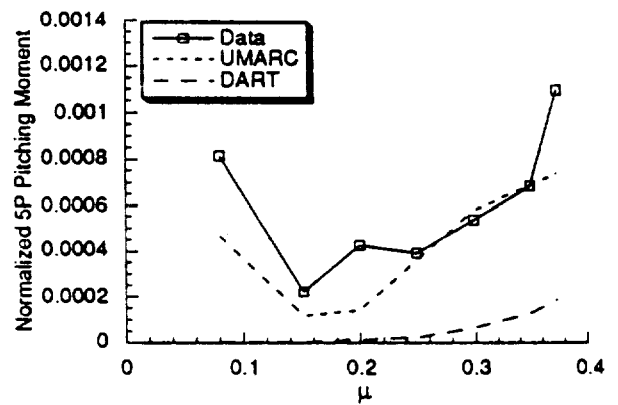


Fig. 14 Comparison of 5P pitching moment data with DART and UMARC results, variation with forward speed at $C_T/\sigma = .076$.